



**HAL**  
open science

# Effective non-halogen flame-retardants combined with nSiO<sub>2</sub> particles to improve thermal stability and fire resistance of high-performance polyurethane nanocomposite foams

Lam Pham, Ngoc Thuy Nguyen, Dang Mao Nguyen, Tuan An Nguyen, Tan Binh Nguyen, Jonghwan Suhr, Tien Dung Nguyen, Mourad Rahim, Anh Dung Tran Le, Lucas Terrei, et al.

## ► To cite this version:

Lam Pham, Ngoc Thuy Nguyen, Dang Mao Nguyen, Tuan An Nguyen, Tan Binh Nguyen, et al.. Effective non-halogen flame-retardants combined with nSiO<sub>2</sub> particles to improve thermal stability and fire resistance of high-performance polyurethane nanocomposite foams. *Journal of Materials Science and Technology*, inPress, 10.1016/j.jmst.2024.02.066 . hal-04530552

**HAL Id: hal-04530552**

**<https://hal.science/hal-04530552>**

Submitted on 2 May 2024

**HAL** is a multi-disciplinary open access archive for the deposit and dissemination of scientific research documents, whether they are published or not. The documents may come from teaching and research institutions in France or abroad, or from public or private research centers.

L'archive ouverte pluridisciplinaire **HAL**, est destinée au dépôt et à la diffusion de documents scientifiques de niveau recherche, publiés ou non, émanant des établissements d'enseignement et de recherche français ou étrangers, des laboratoires publics ou privés.

1 **Effective non-halogen flame-retardants combined with nSiO<sub>2</sub> particles**  
2 **to improve thermal stability and fire resistance of high-performance**  
3 **polyurethane nanocomposite foams**

4 Lam H. Pham<sup>a,b</sup>, Ngoc Thuy Nguyen<sup>a,b</sup>, Dang Mao Nguyen<sup>c\*</sup>, Tuan An Nguyen<sup>a,b</sup>, Tan Binh  
5 Nguyen<sup>d</sup>, Jonghwan Suhr<sup>d,e</sup>, Tien Dung Nguyen<sup>f</sup>, Mourad Rahim<sup>c</sup>, Anh Dung Tran-Le<sup>g</sup>,  
6 Lucas Terrei<sup>h</sup>, Rabah Mehaddi<sup>h</sup>, Yuri Ferreira da Silva<sup>i</sup>, Patrick Perré<sup>i</sup>, DongQuy Hoang<sup>a,b,\*</sup>

7 <sup>a</sup> Faculty of Materials Science and Technology, University of Science, Vietnam National  
8 University, Ho Chi Minh 700000, Vietnam.

9 <sup>b</sup> Vietnam National University, Ho Chi Minh City 700000, Vietnam.

10 <sup>c</sup> Université de Lorraine, LERMAB, 186 Rue de Lorraine, 54400 Cosnes-et-Romain, France

11 <sup>d</sup> Department of Polymer Science and Engineering, Sungkyunkwan University, Suwon-si,  
12 16419, Republic of Korea

13 <sup>e</sup> School of Mechanical Engineering, Sungkyunkwan University, Suwon-si, 16419, Republic  
14 of Korea

15 <sup>f</sup> Institute of Applied Materials Science, Vietnam Academy of Science and Technology, 01B  
16 TL29 District 12, Ho Chi Minh City 700000, Vietnam

17 <sup>g</sup> Laboratory of Technologies Innovative (LTI), University of Picardie Jules Verne, Le  
18 Bailly, 80025 Amiens Cedex, France

19 <sup>h</sup> Université de Lorraine, CNRS, LEMTA, Nancy, F-54000, France

20 <sup>i</sup> Université Paris-Saclay, CentraleSupélec, Laboratoire de Génie des Procédés et Matériaux,  
21 SFR Condorcet FR CNRS 3417, Centre Européen de Biotechnologie et de Bioéconomie  
22 (CEBB), 3 rue des Rouges Terres 51110 Pomacle, France

23 \*Corresponding authors: [dang.nguyen@univ-lorraine.fr](mailto:dang.nguyen@univ-lorraine.fr) (D.M. Nguyen);

24 [htdqy@hcmus.edu.vn](mailto:htdqy@hcmus.edu.vn) (D.Q. Hoang).

## 25 **Abstract**

26 This study focuses on the improvement of the thermal stability and flame-retardant  
27 performance of polyurethane (PU) foam by using effective flame-retardant additives and  
28 nanosilica ( $n\text{SiO}_2$ ) particles from rice husk. The addition of non-halogen flame retardants  
29 (FRs) including aluminum trihydroxide (ATH), triphenyl phosphate (TPP) and  
30 diammonium phosphate (DAP) leads to markedly enhanced thermal stability and fire  
31 resistance of the PU/ $n\text{SiO}_2$ /FRs nanocomposites, resulting in achieving UL-94 HB standard.  
32 In particular, the nanocomposites met the UL-94 V-0 criteria thanks to the inclusion of DAP  
33 at 25 phr. The LOI value of the nanocomposites reached 26% which is much higher than  
34 that of PU/ $n\text{SiO}_2$  nanocomposite, about 20%. In order to further understand the fire-proof  
35 mechanism, the residue char layer remaining of the PU/ $n\text{SiO}_2$ /FRs nanocomposites after  
36 being burned was also investigated by SEM and FTIR. In addition, the microstructure,  
37 thermal stability, thermal conductivity and mechanical properties of nanocomposites were  
38 also evaluated in this study.

39 **Keywords:** Flame retardancy; polyurethane/ $n\text{SiO}_2$  nanocomposite; aluminum hydroxide;  
40 diamonium hydrogen phosphate; thermal stability; nano silica from rice husk.

## 41 **1. Introduction**

42 Polyurethane (PU) foam with outstanding properties such as flexibility in product shaping,  
43 high strength, good sound insulation, and high compressive strength has played an  
44 increasingly important role in many areas of life [1, 2]. However, besides the above  
45 advantages, it still has a disadvantage which is a low fire resistance [3, 4]. This is one of the  
46 main barriers limiting the future development of PU foam materials [5]. To solve this  
47 problem, many solutions have been proposed, but the most widely used is adding flame

48 retardant (FR) additives to PU foam materials [6-9]. Among the FRs used, the most  
49 effective are halogen flame retardants. However, halogen flame retardant additives often  
50 produce a lot of smoke and toxic gases, so now halogen FRs have been banned (or limited)  
51 in many countries around the world. Instead, non-halogen flame-retardant additives (such as  
52 phosphorus-containing compounds, nitrogen-containing compounds, or metal hydroxides)  
53 have shown their ability to effectively replace halogen compounds in the flame-retardant  
54 role for (nano)composite materials based on PU foams [2, 10-13]. Recent advances in  
55 halogen-free FRs for PU foams have focused on three main strategies: inorganic,  
56 phosphorus, and phosphorus-nitrogen FRs. Phosphorus and phosphorus-nitrogen  
57 compounds are effective radical trappers as well as efficient charring agents, acting as flame  
58 retardants in both the gaseous and condensed phases [14-17]. The literatures study that  
59 when both phosphorus and nitrogen were included in the polymers, the flame-retardant  
60 efficacy increased greatly due to the synergistic action of phosphorus and nitrogen. The  
61 incorporation of FRs into composite materials partly improves their fire resistance,  
62 however, this improvement still has many drawbacks. The biggest limitation is that in order  
63 to achieve fire resistance that can be applied in practice, the amounts of FRs are used  
64 relatively large. Especially, in the case of using FRs which are metal hydroxide compounds,  
65 this significantly affects the physical and mechanical properties and also reduces the  
66 applicability of the materials. To overcome this limitation, besides traditional non-halogen  
67 FRs, researchers have proposed to combine inorganic components such as metal oxides  
68 (specifically silica) into a polyurethane foam matrix [10, 18, 19].

69 On the other hand, in the context of the over-exploitation of natural resources, the search for  
70 biological origin materials to increase the sustainability of the final material is also a  
71 concern. For countries that produce a lot of rice, the amount of rice husk (RH) produced

72 every year is extremely large. It is estimated that the amount of RH discharge into the  
73 environment can be up to 100 million tons (in 2018) and it increases over the years [20-22].  
74 In the past, RH was often used as a low-efficiency fuel source, causing great waste because  
75 the source of silica in its components was not utilized [21, 23]. In order to fully utilize the  
76 source of silica present in RH, particularly to improve the fire resistance of PU foam, this  
77 study focuses on using nano silica ( $n\text{SiO}_2$ ) derived from RH combined with non-halogen  
78 FRs to synthesize the effective environmentally friendly flame-retardants which could be  
79 used to enhance the thermal stability and fire retardancy for PU foams. In the past recent  
80 years,  $n\text{SiO}_2$  has been widely integrated into polymer materials to improve heat resistance,  
81 radiation resistance, mechanical, and flame retardancy properties [24-27]. During  
82 combustion,  $n\text{SiO}_2$  has the ability to catalyze the creation of carbonaceous carbon on the  
83 surface. This carbon layer can play a role as a barrier, keeping the underlying material from  
84 coming into touch with the flame and therefore limiting the fire propagation. Besides that,  
85 the addition of  $n\text{SiO}_2$  decreased the heat release rate and total heat release of the material  
86 [28, 29]. The spread of fire also can be delayed by limiting the quantity of heat emitted  
87 during combustion.

88 However, the use of  $n\text{SiO}_2$  has a limitation in terms of improving the flame retardancy for  
89 PU foam because the action of mechanism is attributed to condensed phase/physical effect  
90 that improves the thermal stability and low thermal conductivity rather than gas  
91 phase/chemical reaction [30]. To fulfill the requirements of many applications that demand  
92 a high degree of flame retardancy, it is necessary to incorporate FR additives to slow down  
93 or potentially extinguish the burning process. While numerous studies have explored the  
94 incorporation of non-halogen FRs into fire-proof PU nanocomposite foams, there is a  
95 limited literature addressing the improvement of the thermal stability and flame-retardant

96 performance of PU nanocomposite foam by using effective non-halogen FR additives and  
97 nSiO<sub>2</sub> from RH.

98 In this study, we used three types of FRs: phosphorus FR (TPP), nitrogen-phosphorus FR  
99 (DAP), and inorganic FR (ATH). According to the flame-retardant mechanism FRs are  
100 classified into two types: chemical and physical mechanisms. While ATH works mainly  
101 according to the physical mechanism, releasing water and forming Al<sub>2</sub>O<sub>3</sub> in the condensed  
102 phase [31]. On the contrary, TPP works mainly by chemical mechanism, during combustion  
103 TPP retards flames by producing phosphoric acids during the pyrolysis process and  
104 releasing phosphorus-containing radicals, breaking the chain reaction of combustion [32].  
105 And more especially DAP which could act to chemical and physical mechanisms. DAP  
106 achieves its fire resistance by slowing down heat and fuel transfer processes during polymer  
107 combustion through dilution effect, while phosphorus-containing moieties active free  
108 radicals transferred from phosphorus derivatives could deactivate H• and OH• radicals.  
109 Furthermore, the char formation through pyrophosphoric acid also contributes to the  
110 polymer materials' flame retardancy [33].

## 111 **2. Experimental**

### 112 **2.1. Material**

113 Methylene diphenyl diisocyanate (MDI) (DESMODUR 44 V 20 L) containing less than  
114 31% NCO was supplied by DOW, China. Its viscosity and density are 210 mPa and 1.23  
115 g/cm<sup>3</sup> at 25 °C, respectively. Polyol (Voracor CR 765) was purchased from DOW, China  
116 with OH index of 360 mg KOH/g, viscosity of 800 mPas, and density of 1.12 g/cm<sup>3</sup> (at 20  
117 °C). Rice husk was provided from a rice mill in the Mekong Delta of Vietnam. HCl 37%  
118 was purchased from Xilong, China. Flame retardant additives: triphenyl phosphate (TPP)

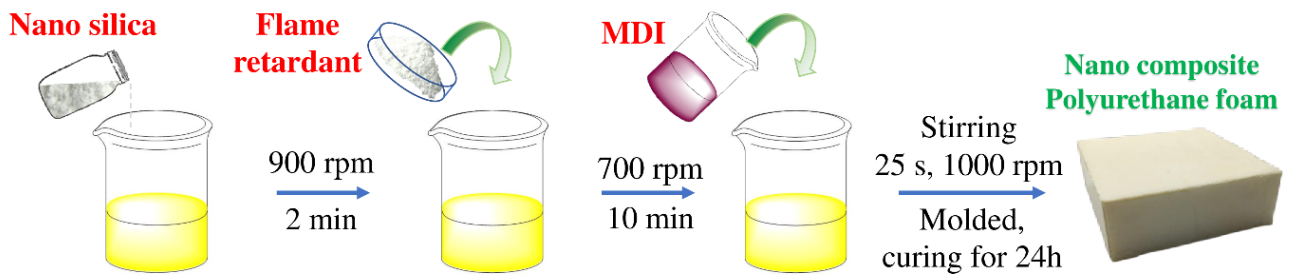
119 was supplied by Merck, Germany. Diamonium hydrogen phosphate (DAP) and aluminum  
120 trihydrate (ATH) were purchased from Guangdong Guanghua Sci-Tech Co., Ltd.,  
121 Guangdong, China.

## 122 **2.2. Synthesis of nSiO<sub>2</sub> from rice husk**

123 The nSiO<sub>2</sub> is synthesized using the same procedure as reported in previous work [34]. To  
124 remove contaminants, RH was washed in water and dried at 60 °C. Then, the RH was  
125 treated with 500 ml of 1% HCl at room temperature for 2 h using a mechanical stirrer. The  
126 mixture was given an overnight soak before being completely cleaned with distilled water to  
127 a pH of 7. It was then dried to constant mass. The RH was then milled into a fine powder  
128 and burnt at 700 °C for 2 h in a furnace to collect nSiO<sub>2</sub>.

## 129 **2.3. Preparation of PU foam/nSiO<sub>2</sub>/FRs nanocomposites**

130 PU foam/nSiO<sub>2</sub>/FRs nanocomposites are synthesized on the one-pot method as described in  
131 Figure 1. Accordingly, Figure 1 depicts the steps taken in the manufacture of a  
132 nanocomposite PU/nSiO<sub>2</sub> with and without flame retardant additive. Accordingly, nSiO<sub>2</sub>  
133 was first added to the polyol and stirred to completely disperse for 2 min. Then the FR was  
134 added and stirred to obtain the homogeneous dispersion mixture. After that, MDI was  
135 quickly added to the mixture and thoroughly stirred for about 20–25 s. Then, the mixture  
136 was quickly poured into the mold, with the dimension of 150 × 150 × 50 mm, the lid of the  
137 mold was quickly closed then. The mold was kept closed to ensure that the nanocomposite  
138 was completely cured. The sample was kept stable in the mold for 24 h at room temperature  
139 before preparing for further evaluation.



140

141

**Figure 1.** Procedure to prepare PU foam/nSiO<sub>2</sub>/FRs nanocomposite.

142

## 2.4. Characterization

143

The fire resistance of the materials was tested using the UL-94 V and UL-94 HB methods.

144

The dimension of each specimen bar is 127 × 13 × 10 mm and the test procedure has been

145

performed in accordance with ASTM D635 and ASTM D3801 with UL-94 HB and UL-94

146

V methods, respectively. In addition to UL-94, limiting oxygen index (LOI) is also a very

147

popular method to test the fire resistance of materials. The measurement of LOI value was

148

carried out according to ASTM D2863, with a sample dimension of 130 × 10 × 10 mm.

149

The fire reaction at the material scale were also performed with a cone calorimeter oriented

150

vertically. The experiment consists of exposing a sample to a radiant heat flux coming from

151

an electrically heated conical coil [35]. The samples were exposed vertically to the radiant a

152

heat flux of  $50 \pm 0.5 \text{ kW.m}^{-2}$  without pilot. The radiant heat flux emitted by the cone was

153

controlled before each test using a Schmidt-Boelter fluxmeter (Medtherm). The selected

154

sample sizes were 100×100 mm with a 10 mm thickness. As specified in the standard ISO

155

5660-1 [36], the samples were wrapped with two layers of aluminum foil, except their top

156

side exposed to the radiative heat flux. The sample was then placed in a steel holder,

157

followed by ceramic insulating foam and ceramic plate. The distance between the sample

158

and the heater was 25 mm. A precision scale with a 0.01 g resolution was used to measure

159 the mass loss. The mean mass loss and the Mass Loss Rate Per Unit Area (MLRPUA) are  
160 the average of three measurements.

161 The thermal properties of nanocomposite with and without flame retardant additives were  
162 tested using LABSYS EVO machine (DTA/DSC-1600 °C) (Setaram, France). The samples  
163 are analyzed in the temperature range of 25–800 °C, with a heating rate of 10 °C/min in the  
164 N<sub>2</sub> gas environment.

165 The density of the nanocomposite was determined according to EN 323 standard, at least 3  
166 specimens of each nanocomposite with size 50 × 50 × 50 mm were prepared and measured.

167 The compressive property of the nanocomposite was performed in the direction parallel to  
168 the rising foam using a Mechanical Tester model AG-X plus (Shimadzu, Japan) with a  
169 compression speed of 2.5 mm/min according to ASTM D1621 standard. The results  
170 obtained are the average of 5 measurements for each nanocomposite.

171 The nanocomposites and their residue chars after burning at 500 °C were evaluated by a  
172 scanning electron microscope (SEM, Hitachi S-4300, Tokyo, Japan) at a voltage of 15 kV.

173 The samples were coated with platinum before scanning.

174 Moreover, microscopic images of nanocomposites were also obtained using an  
175 environmental scanning electron microscope (ESEM, Quanta 200, FEI Company). Two  
176 sample preparations were tested: a surface cut by a microtome blade and a fracture surface.

177 The latter yielded better results and was adopted for all samples. The samples were placed  
178 on carbon conductive double-sided adhesive disc, without any further preparation. Images  
179 were taken in Low Vac mode at 100 Pa, with a 10 kV voltage, a beam spot size of 4.5 and a  
180 working distance of approximately 10 mm. The Low Vac mode allows samples to be  
181 imaged without any coating even though they are not electrically conductive. The tension

182 was reduced to limit the beam penetration and the working distance was a compromise  
183 between the detector signal and the degradation of the electron beam in the chamber.

184 The quantification of pore dimensions was performed in FIJI (Image J version 1.54f) [37]  
185 using the Local Thickness tool. In this method, the algorithm determines the diameter of the  
186 largest circle that can be fit inside an object. To this end, regions of 800 x 800 pixels were  
187 selected from each image. Brightness and contrast were automatically corrected, and the  
188 “Find Edges” command was applied. The resulting images were inverted and later  
189 processed using the “Local Thickness” command. Histograms were plotted using the values  
190 from the thickness maps.

191 Raman spectra were obtained in an Alpha 300R Plus equipment (Witec, Germany) using a  
192 785 nm laser and a 10x objective lens (EC Epiplan Neofluar, ZEISS, Germany) with a  
193 numerical aperture of 0.25. Spectra were measured on three regions of the sample fracture  
194 surface, with an integration time of 0.5 s and 100 accumulations. The replicate spectra were  
195 averaged and processed in RStudio (version 2023.09.1) using the hyperSpec package [38].  
196 Spectra were smoothed using a second order Savitsky-Golay filter with an 11-point  
197 window. Also, a linear baseline correction has been performed. Specifically, hyperspectral  
198 maps were generated for 250 x 250  $\mu\text{m}^2$  regions from the PU-nSiO<sub>2</sub>/<sup>β</sup>5TPP sample. The  
199 chemical images were obtained over a total of 50 x 50 points with an integration time of 0.1  
200 s. Maps of integrated intensity for two regions (1604-1624  $\text{cm}^{-1}$  and 998-1018  $\text{cm}^{-1}$ ) were  
201 plotted using Witec Project FOUR software (Build 4.0.18.15).

202 nSiO<sub>2</sub> was analyzed on an X-ray diffractometer, D8 Advance A25 (Bruker, Karlsruhe,  
203 Germany), using Cu K<sub>α</sub> radiation, and the 2 Theta between 10° and 80°. The particle size  
204 and morphology of the nSiO<sub>2</sub> were investigated by transmission electron microscopy  
205 (TEM), model JEM1400 (JEOL, Tokyo, Japan).

206 The FTIR-ATR spectrum was recorded using a diamond crystal and an incident angle of 45°  
207 (JASCO FT/IR-6600). For each sample, an average of 32 scans with a 16 cm<sup>-1</sup> resolution  
208 were carried out in the 400–4000 cm<sup>-1</sup> wavenumber range.

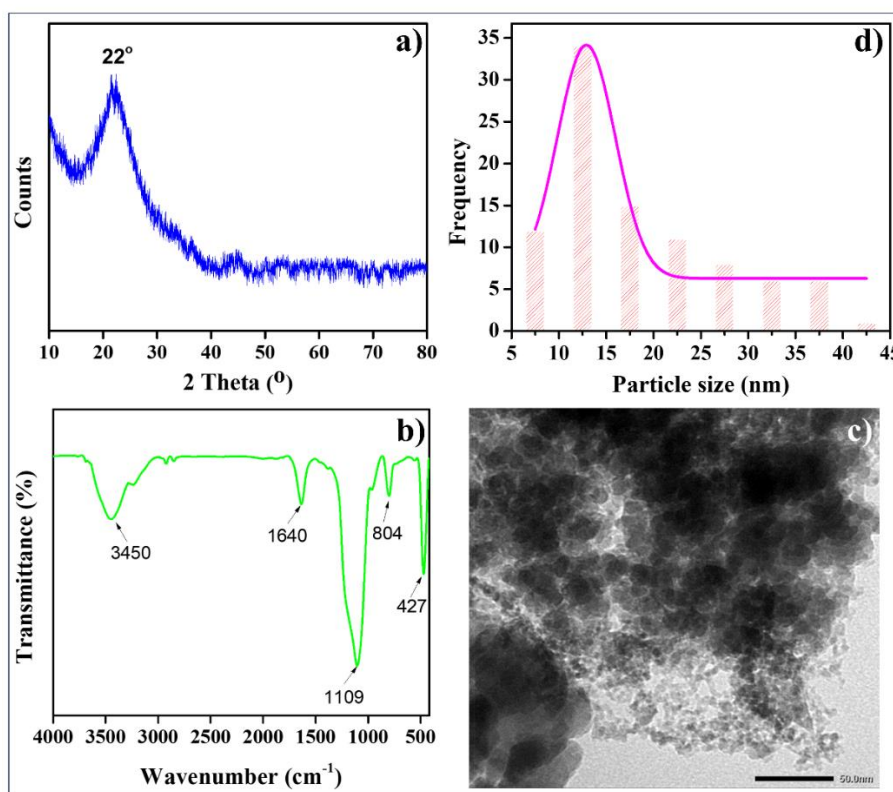
209 In order to characterize the thermal conductivity of studied materials, the Hot Disk TPS  
210 2200 (the Hot Disk method, also referred to as the Transient Plane Source, TPS or the  
211 Gustafsson Probe), has been used. The measurements were performed in a climate chamber  
212 where temperature and relative humidity were maintained at 23°C and 50 % RH,  
213 respectively. The Hot Disk sensor 7577 (r =2 mm) has been used and was placed between  
214 two identical samples being tested with dimensions of 50 × 50 × 5 mm. Three  
215 measurements were done for each sample; the thermal conductivity presented in this article  
216 is an average value from 3 measurements.

### 217 **3. Results and discussion**

#### 218 **3.1. Properties of nSiO<sub>2</sub>**

219 Prior to burning, RH was treated by HCl to remove inorganic impurities like Fe, Mn, Ca,  
220 Na, K, and Mg, which can affect the material properties. The treatment of RH with HCl acid  
221 was carried out at room temperature with a 1% (w.w<sup>-1</sup>) HCl concentration. Following HCl  
222 treatment, the RH was cleaned with distilled water before being dried at 60 °C to a constant  
223 weight. The nSiO<sub>2</sub> sample was then produced by burning RH powder (after HCl treatment)  
224 at 700 °C for 2 h. This removed all organic chemicals present in the RH components  
225 (cellulose, hemicellulose, and lignin). The obtained nSiO<sub>2</sub> sample is a white powder. The  
226 characteristics of the nSiO<sub>2</sub> were evaluated using XRD, FTIR, and TEM methods (Figure  
227 2). The burning of RH can produce either amorphous nSiO<sub>2</sub> or crystalline forms of SiO<sub>2</sub>,  
228 depending on the temperature conditions [39]. The nSiO<sub>2</sub> produced by burning RH at 700  
229 °C was found to be in an amorphous state (the peak at 2 Theta: 22°), which is consistent

230 with the XRD of nSiO<sub>2</sub> presented in Figure 2a. The FTIR spectrum of the SiO<sub>2</sub> sample,  
231 which was acquired after burning the RH sample treated with HCl at 700 °C for 2h, is  
232 shown in Figure 2b. A low-intensity signal peak is presented at wavenumber 1640 cm<sup>-1</sup>, this  
233 signal is caused by the bending vibration of the linkage Si-OH [40]. At a wavenumber of  
234 3450 cm<sup>-1</sup>, there is a signal associated with the stretching of the O-H group. Particularly, the  
235 FTIR result of the nSiO<sub>2</sub> exhibits signal peaks that are attributed to the asymmetric  
236 stretching vibration of O-Si-O in the wavenumber of 1109 cm<sup>-1</sup>, the symmetric stretching  
237 vibration of O-Si-O at 804 cm<sup>-1</sup>, and the bending vibration of O-Si-O at 472 cm<sup>-1</sup> [41]. TEM  
238 was used to examine the size and form of the nSiO<sub>2</sub> particles obtained from RH. The  
239 particle size distribution chart (Figure 2c) and the transmission electron microscopy image  
240 (Figure 2d) both show silica particles with spherical shapes. As can be observed, the  
241 average size of the silica particles is about 10–15 nm.



242

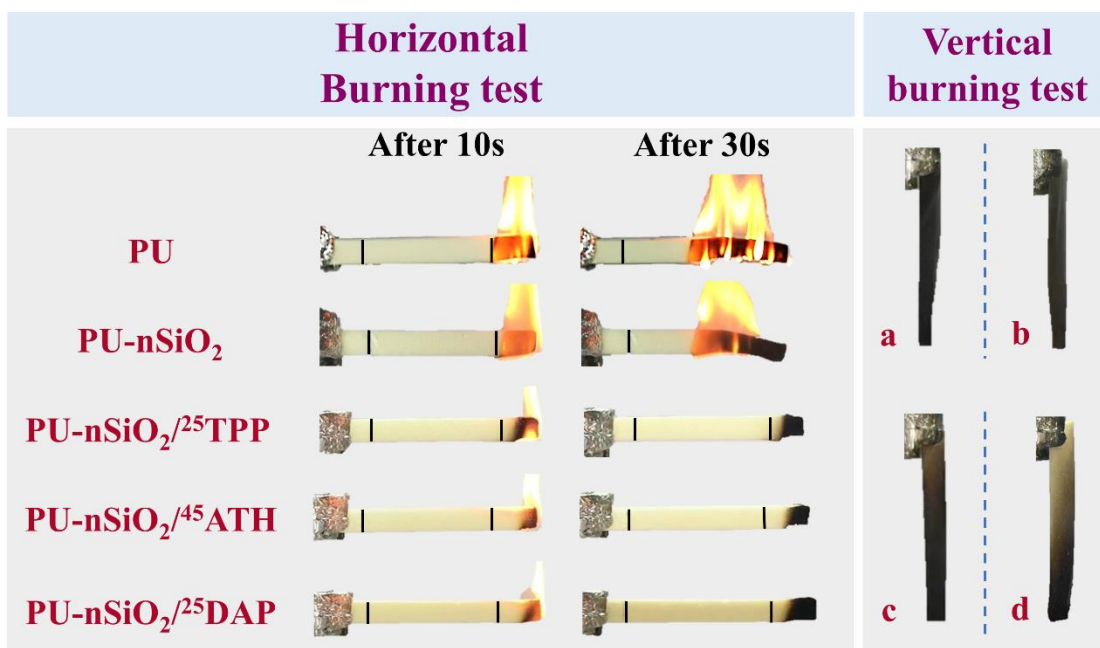
243 **Figure 2.** a) XRD, b) FTIR, c) TEM image, and d) Particle size distribution diagram of

244

nSiO<sub>2</sub>.

245 **3.2. Flame retardancy**

246 The flame retardancy of rigid PU foam and PU-nSiO<sub>2</sub> nanocomposite foam with and  
247 without flame retardant additives was tested using both the UL-94 HB and UL-94 V tests.  
248 The samples are initially evaluated for UL-94 HB, and if that standard is reached, the  
249 samples are then subjected to UL-94 V testing. Table 1 and Figure 3 show the UL-94 HB  
250 test results.



251 a) PU-nSiO<sub>2</sub>/<sup>25</sup>TPP; b) PU-nSiO<sub>2</sub>/<sup>35</sup>TPP; c) PU-nSiO<sub>2</sub>/<sup>45</sup>ATH; d) PU-nSiO<sub>2</sub>/<sup>25</sup>DAP

252 **Figure 3.** Result of UL-94 testing of rigid PU and PU-nSiO<sub>2</sub> with and without FR.

253 The rigid PU foam sample burnt swiftly past the 25 mm (1 inch) mark after only a few  
254 seconds of exposure to the heat of the flame. After ceasing to burn, the flame continues to  
255 spread and burn out the sample, producing a large amount of smoke. After burning the  
256 sample is completely deformed. For the PU-nSiO<sub>2</sub> sample without flame retardant,  
257 performing the UL-94 HB test also gave a similar result. Fire behavior is greatly improved  
258 with the addition of FR compounds. The flame has not yet reached the initial 25 mm mark  
259 in the presence of DAP additive at 25 phr, in the 30 s of burning time, and the flame is

260 extinguished as soon as it stops burning. Similar results were observed after the addition of  
 261 TPP at 25 phr or ATH at 45 phr (Table 1, Figure 3). However, compared to TPP, DAP, and  
 262 ATH flame retardants dramatically reduced the amount of smoke generated during the UL-  
 263 94 HB test. It is clear that the composite material was able to meet the UL-94 HB fire  
 264 resistance criteria thanks to the introduction of FR additives.

265 **Table 1.** Flame retardancy performance of rigid PU and PU-nSiO<sub>2</sub> with and without FR.

Sample	FR loading (phr)	Combustion test		LOI (%)
		Horizontal burning	Vertical burning	
PU	0	Not achieved	No rating	-
PU-nSiO <sub>2</sub>	0	Not achieved	No rating	20
PU-nSiO <sub>2</sub> / <sup>25</sup> TPP	25	HB	No rating	-
PU-nSiO <sub>2</sub> / <sup>35</sup> TPP	35	HB	V-1	-
PU-nSiO <sub>2</sub> / <sup>40</sup> ATH	40	HB	V-1	-
PU-nSiO <sub>2</sub> / <sup>45</sup> ATH	45	HB	V-0	24
PU-nSiO <sub>2</sub> / <sup>20</sup> DAP	20	HB	V-1	-
PU-nSiO <sub>2</sub> / <sup>25</sup> DAP	25	HB	V-0	26

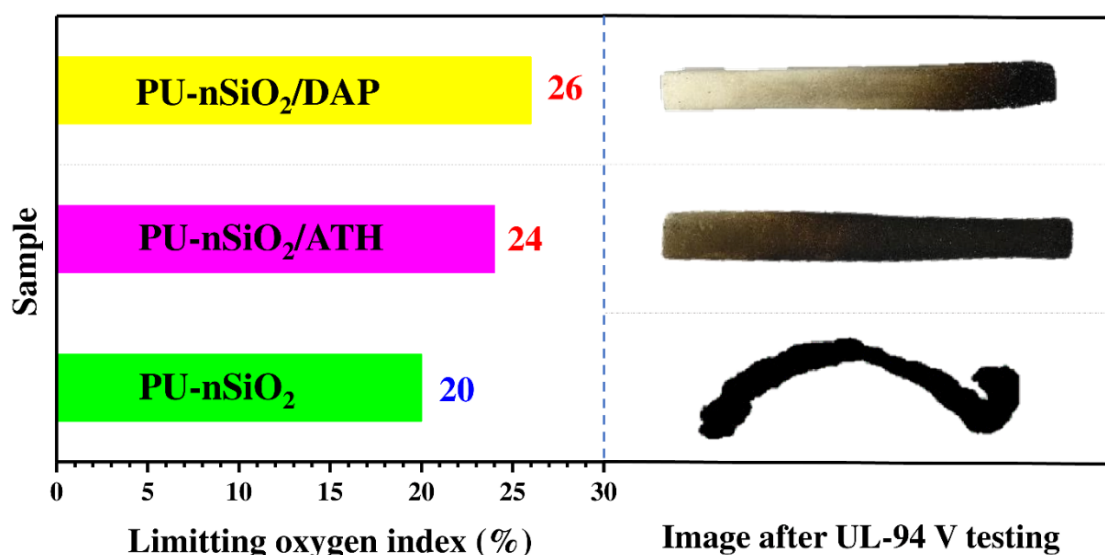
266 *The ratio of polyol/isocyanate:1/1.5 (g/g); nSiO<sub>2</sub>:3 wt%*

267 Based on the UL-94 HB test results just reported, the UL-94 V test is further used to  
 268 evaluate the fire resistance of the nanocomposites in the presence of FR additives. For the  
 269 sample containing TPP with a content of 25 phr, the flame was extinguished immediately  
 270 after the first 10 s of burning, the sample was continuously burned for 10 s and the sample  
 271 was stopped without further burning. However, during the burning time, the flame reached  
 272 the specimen holder, and the specimen was deformed after combustion, producing a lot of  
 273 smoke, and deformation appeared (Figure 3). As can be seen from the result of the UL-94  
 274 HB test, the addition of TPP flame retardant at 25 phr improves the fire resistance (the

275 sample has achieved UL-94 HB), but it is ineffective in achieving the UL-94 V-0 standard.  
276 Increasing the content of TPP flame retardant additive to 35 phr has proven to be effective,  
277 the material doesn't deform too much after testing the fire resistance by the UL-94 V  
278 method, but the issue with fire to the specimen holding clamp is still present (Figure 3).  
279 Therefore, even after raising the amount of TPP used to 35 phr, the sample did not satisfy  
280 the UL-94 V-0 standard because TPP acts as a plasticizer in addition to its flame-retardant  
281 effect [38]. Increasing the TPP additive content to 35 phr has affected the shape, physical,  
282 and mechanical properties of the nanocomposites as well as the shrinkage of the samples  
283 after synthesis. For the nanocomposite containing ATH additive at a content of 45 phr, the  
284 flame extinguishes instantly after ceasing to burn after 10 s of the first burning and 10 s of  
285 the second burning, according to UL-94 V test results (Figure 3). Moreover, the specimen  
286 was not deformed after burning, and less smoke was produced than that of the  
287 nanocomposite containing TPP and without flame retardant additive. The presence of DAP  
288 additive with 25 phr content in the nanocomposite gets the best UL-94 V test results among  
289 all the samples containing the flame retardant studied. When the sample was exposed to the  
290 heat source during both combustion durations, it was not burned up to the specimen holding  
291 clamp and self-extinguished immediately after it stopped burning. Moreover, the amount of  
292 smoke generated during combustion was also significantly lower than when using ATH and  
293 TPP additives (Figure 3). The results show that the use of ATH at 45 phr and DAP at 25 phr  
294 in PU foam nanocomposites allows them to meet the criteria of the UL-94 V-0 flame  
295 retardant standard.

296 In addition to the UL-94 test method, the limiting oxygen index (LOI) test method was also  
297 conducted with samples with ATH or DAP and without flame retardant to verify the flame-  
298 retardant properties of the additives DAP and ATH. The LOI test results shown in Tables 1

299 and Figure 4 are very consistent with the UL-94 test results. The LOI value of the  
300 nanocomposite without flame retardant compounds reached 20%. This LOI value is  
301 classified as combustible material due to the porous structure of PU foam, which makes it  
302 very flammable, little nSiO<sub>2</sub> was utilized (3 wt%), which was insufficient to decrease the  
303 flammability of the base plastic when the flame spread swiftly.



304

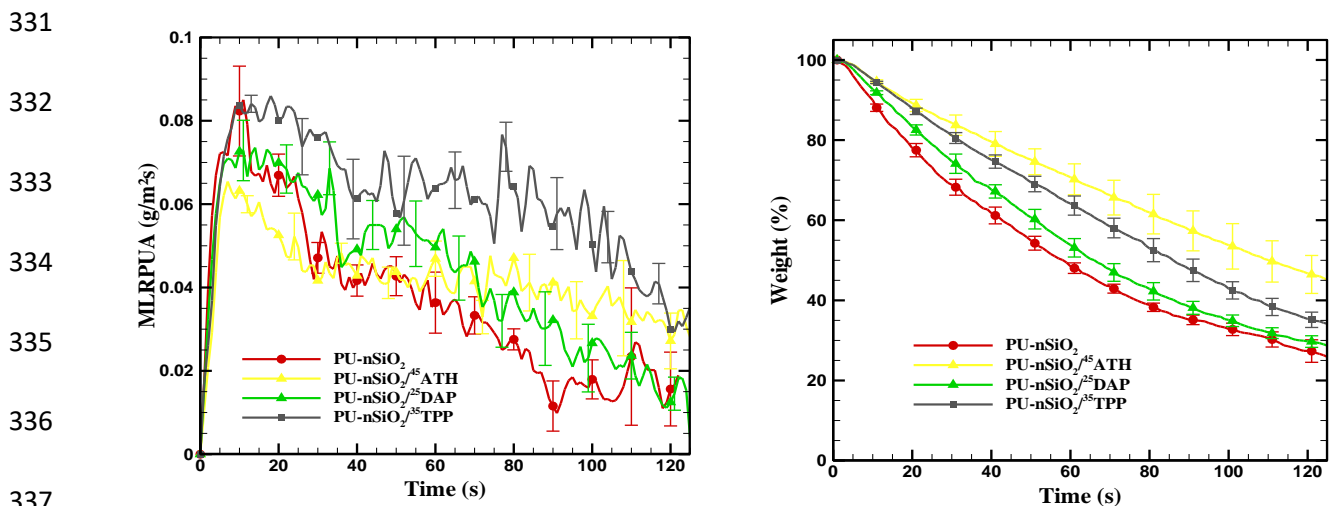
305

**Figure 4.** Resulting of LOI test of the nanocomposites.

306 The introduction of ATH and DAP significantly increased the LOI value of the  
307 nanocomposites. The LOI value of the sample, specifically, reached 24% and 26%  
308 respectively when adding ATH additive at 45 phr or DAP additive at 25 phr (both LOI  
309 values above are classified as self-extinguishing materials). The results of LOI and UL-94  
310 demonstrate that the presence of ATH and DAP flame retardant additives greatly increased  
311 the flame retardancy of the nanocomposites.

312 A cone calorimeter test was carried out to investigate the combustion behavior of samples  
313 with and without FR. In comparison with TGA, this kind of experiment allows to explore  
314 larger-scale effects such as heat transfer through the sample and the formation of char at the  
315 surface of the sample. The results, including the MLRPUA and mass loss, are shown in

316 Figure 5a and Figure 5b, respectively. Accordingly, the average MLRPUA of the PU-nSiO<sub>2</sub>  
 317 sample at an incident heat flux of 50 kW m<sup>-2</sup> in cone calorimeter increases with a peak of  
 318 0.085 gm<sup>-2</sup>s<sup>-1</sup> and then decreases sharply with time. At 120 s, the MLRPUA data is close to  
 319 0.015 gm<sup>-2</sup>s<sup>-1</sup> and the total mass loss is about 74% (Figure 5b). The peak of MLRPUA for  
 320 the PU-nSiO<sub>2</sub>/<sup>35</sup>TPP sample is similar to that of the PU-nSiO<sub>2</sub> sample, but this value then  
 321 decreases slowly with time. At 120 s, the MLRPUA data of this sample is nearly 0.03 gm<sup>-2</sup>  
 322 s<sup>-1</sup> and the total mass loss is about 65%. Compared to the PU-nSiO<sub>2</sub> sample, the  
 323 incorporation of 35 phr TPP maintains a similar MLRPUA peak, but the TPP leads to a  
 324 relatively faster decay of the MLRPUA profile. The MLRPUA peak of the PU-nSiO<sub>2</sub>/<sup>25</sup>DAP  
 325 sample is at 0.0727 gm<sup>-2</sup>s<sup>-1</sup>. Over 120 s, the MLRPUA data of this sample is almost 0.0125  
 326 gm<sup>-2</sup> s<sup>-1</sup> and the total mass loss is about 70% (Figure 5b). Compared to the PU-nSiO<sub>2</sub>  
 327 sample, the incorporation of 25 phr DAP lowered the MLRPUA peak but kept nearly the  
 328 same decay of the MLRPUA profile. Finally, the peak of MLRPUA for the PU-  
 329 nSiO<sub>2</sub>/<sup>45</sup>ATH sample is lower with a value of 0.065 gm<sup>-2</sup>s<sup>-1</sup>. At 120 s, the MLRPUA data of  
 330 this sample is nearly 0.0275 gm<sup>-2</sup>s<sup>-1</sup> and the total mass loss is about 55%.

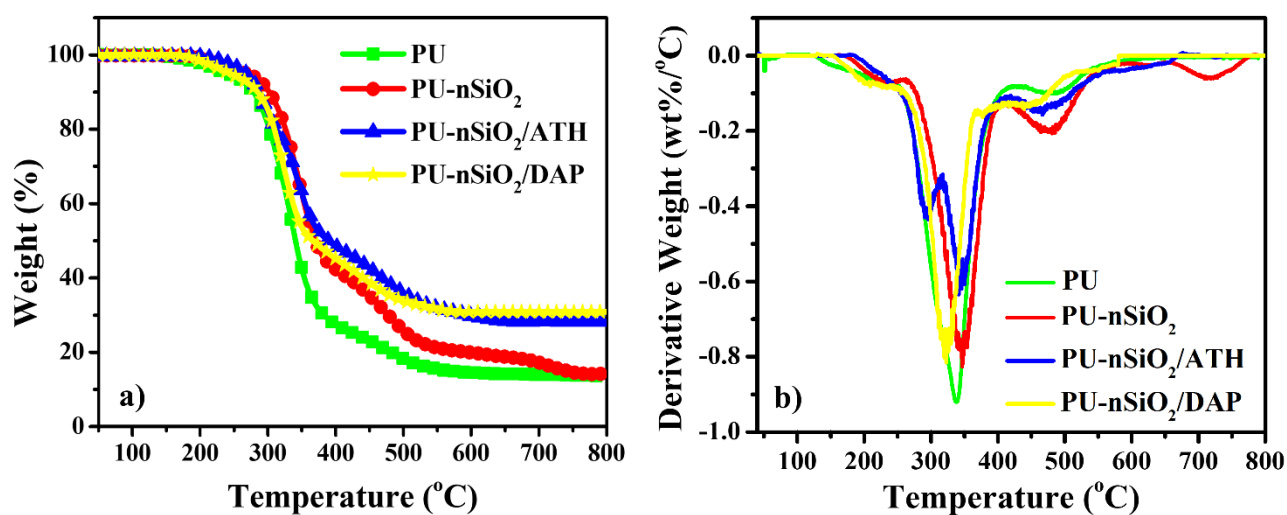


338 Figure 5. The experimental cone calorimeter tests for mass loss rate per unit area  
 339 (MLRPUA) (a) and mass loss (b) of the samples at an external heat flux of 50 kW.m<sup>-2</sup>.

340 Accordingly, the incorporation of 45 phr ATH led to a lower MLRPUA peak. The  
341 significant reduction of MLRPUA peak could be explained by the thin char layer formed  
342 above the sample surface during the cone calorimeter test. Thus, the presence of DAP (25  
343 phr) and ATH (45 phr) in the nanocomposite led to improve fire resistance through the  
344 reduction of the MLRPUA peak during the combustion. Moreover, the mass loss of these  
345 samples is small in comparison with the PU-nSiO<sub>2</sub> sample, which does not contain flame-  
346 retardant additives.

### 347 3.3. Thermal properties

348 The thermal characteristics of the nanocomposites have been evaluated by Thermo-  
349 Gravimetric Analysis (TGA). Figure 6 shows the TGA and DTG curves for the  
350 nanocomposites with and without flame retardant additives in the range of room  
351 temperature to 800 °C, at a rate of 10 °C/min in a N<sub>2</sub> gas environment. Table 2 summarizes  
352 information obtained from TGA including T<sub>5</sub>, T<sub>50</sub>, and T<sub>65</sub> respectively the temperature at  
353 which the sample lost 5, 50, and 65% of the weight and the residue char at 800 °C.



354 **Figure 6.** (a) TGA and (b) DTG curves of PU and PU-nSiO<sub>2</sub> nanocomposite with and without FR.

355 The sample without flame retardant additives exhibits three primary stages of heat  
356 degradation, as shown by the TGA curve in Figure 6. The first stage of thermal  
357 decomposition occurs in the temperature range of 300–360 °C with a large mass loss (about  
358 55% of sample mass). This procedure is the breakdown of the polyol long chains and the  
359 urea bond. At the second stage of thermal decomposition, which lasts between 370 and 550  
360 °C, 25% of the mass was lost. During this stage, the cross-links and aromatic ring bonds of  
361 the porous PU are broken. The thermostable aromatic compounds that are produced during  
362 the second decomposition completely decompose in the third stage of the process, which  
363 takes place at temperatures between 675 and 750 °C [11]. The mass of the sample was  
364 almost constant between 750 and 800 °C. The amount of residual char at 800 °C was about  
365 14 % of the initial sample weight (Table 2). Comparing the TGA results of PU foam and PU  
366 foam/nSiO<sub>2</sub> nanocomposites, it was found that the presence of nSiO<sub>2</sub> (even at a very low  
367 content, 3 wt%) significantly increased the thermal stability of PU materials. The T<sub>5</sub>, T<sub>50</sub>  
368 and T<sub>65</sub> values of the nanocomposites are all higher than that of the PU foam. The reason for  
369 this result may be due to the amount of nSiO<sub>2</sub> added has been evenly distributed in the PU  
370 foam matrix, and when the nanocomposite was exposed to heat, nSiO<sub>2</sub> creates a barrier  
371 layer char that protects the inside material and makes the material more thermally stable.  
372 Indeed, the presence of nSiO<sub>2</sub> acts mainly as a delay of thermal degradation: the ultimate  
373 residual mass, at 800 °C, is the same as the net PU foam. In addition, due to the relatively  
374 small nSiO<sub>2</sub> content, it is impossible to effectively protect the sample from the impact of the  
375 flame or improve remarkable thermal properties.

376 **Table 2.** Thermal stability parameters of the nanocomposites from TGA analysis.

Sample	Temperature (°C)			Residue at 800 °C (%)
	T <sub>5</sub>	T <sub>50</sub>	T <sub>65</sub>	

PU	236	341	363	13.2
PU-nSiO <sub>2</sub>	269	370	451	14.2
PU-nSiO <sub>2</sub> / <sup>25</sup> DAP	244	367	483	30.8
PU-nSiO <sub>2</sub> / <sup>45</sup> ATH	268	389	508	28.3

377 As seen in Figure 6, the thermal degradation of the nanocomposite with ATH content of 45  
378 phr proceeds in two stages. The first decomposition stage comes at temperatures between  
379 250 and 370 °C, with a mass loss of roughly 45%. Most of the mass loss at this stage is due  
380 to the degradation of the ATH additive. At temperatures greater than 210 °C, ATH begins to  
381 decompose to produce aluminum oxide and water, which evaporates at high temperatures  
382 [42]. Parallel to the above-mentioned process, the decomposition of the urea bond also  
383 occurs. The second stage of thermal decomposition takes place at a temperature of 380–520  
384 °C, and the sample loses about 25% of the mass, at this time, the sample with ATH additive  
385 was decomposed the cross-links, aromatic ring links derived from isocyanate. As can be  
386 shown in Table 2, the T<sub>50</sub> and T<sub>65</sub> values of the PU-nSiO<sub>2</sub>/ATH sample are both larger than  
387 that of the PU-nSiO<sub>2</sub> sample (389 and 508 °C versus 370 and 451 °C, respectively). It is  
388 obvious that the sample with ATH additive considerably enhanced the thermal stabilization  
389 in stage 2 of proceed decomposition as compared to the sample without additive. The cause  
390 of this is the effectiveness of the aluminum oxide layer and the nSiO<sub>2</sub> layer acts as a  
391 protective barrier to block heat transmission and mass transfer, assisting in more  
392 successfully protecting the sample. After 660 °C, the sample is stable and its weight is  
393 practically unchanged. The amount of residual char in the sample at 800 °C reached 28% of  
394 the sample weight, twice as high as the residual char of the PU-nSiO<sub>2</sub> sample. The presence  
395 of ATH therefore not only delays the temperature levels at which decomposition arises but  
396 also reduces very significantly the total mass loss.

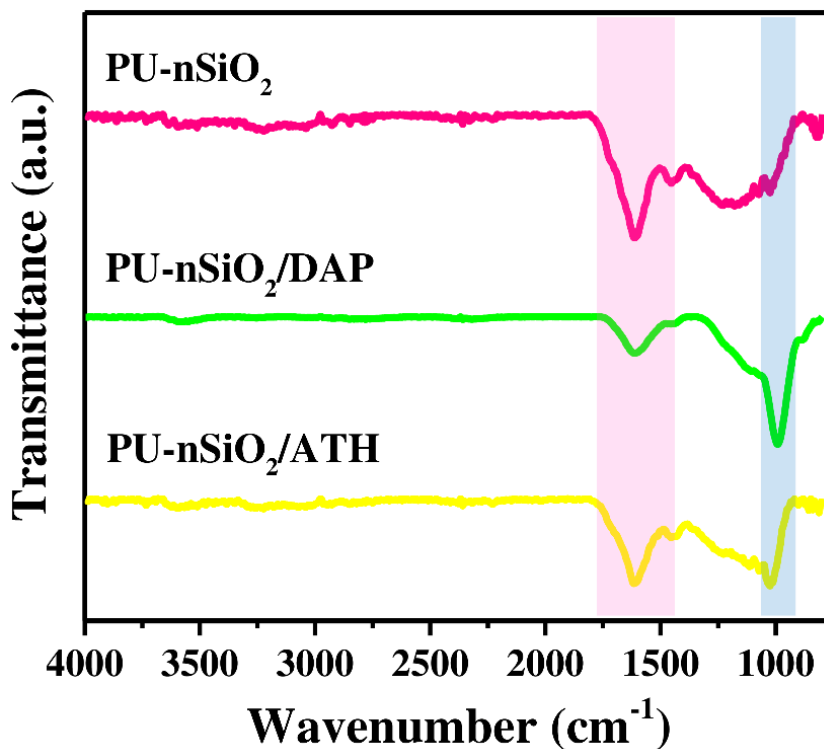
397 Two distinct stages of thermal degradation can be observed in Figure 6 for the  
398 nanocomposite with the addition of DAP additive. At the first stage of thermal  
399 decomposition, which took place between 280 and 370 °C, 51% of the sample mass was  
400 lost. The presence of DAP made the thermal degradation stage in nanocomposites occur  
401 earlier when compared to the nanocomposite sample without flame retardant additive. The  
402 cause of this phenomenon is that DAP is decomposed to produce water vapor and ammonia  
403 gas, accompanied by a layer of solid char  $P_4O_{10}$  [33]. It is the early degradation of DAP that  
404 significantly increases the thermal stability of the nanocomposites, thereby effectively  
405 protecting the material in the second stage of decomposition. In the subsequent thermal  
406 decomposition process, from 390 to 500 °C, 12% of the mass of the nanocomposite sample  
407 was lost as a result of the breakdown of the crosslink and the bonding of the aromatic ring  
408 present in the MDI structure. The sample lost less weight than the nanocomposite with the  
409 ATH additive and the nanocomposite without the additive because the residual char  $P_4O_{10}$   
410 layer, created by the DAP additive, combined with  $nSiO_2$ , effectively protected the  
411 underlying material from thermal degradation. Specifically, the sample is thermal stable and  
412 the mass remains constant from 580 °C forward (while with the nanocomposite sample  
413 containing the ATH additive and the nanocomposite without the FR, the temperature at  
414 which the sample mass remains constant is 660 °C and 750 °C, respectively). The sample  
415 with DAP has more residual char at 800 °C, 31% of the initial mass, as compared to 28%  
416 and 14% for the two nanocomposites with ATH additive and without flame retardant,  
417 respectively. This outcome demonstrates that the thermal stability of nanocomposite  
418 materials is markedly improved by the introduction of DAP flame retardant component.

419

420

421 **3.4. Characterization of the residual char**

422 FTIR has been used to analyze the residual chars generated after burning the samples at 500  
423 °C, as shown in Figure 7.

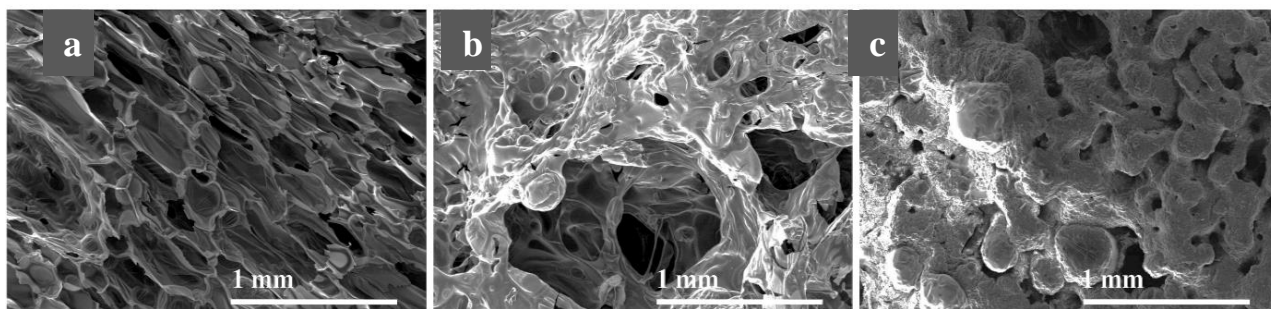


424

425 **Figure 7.** FTIR spectra of PU-nSiO<sub>2</sub>, PU-nSiO<sub>2</sub>/<sup>25</sup>DAP, and PU-nSiO<sub>2</sub>/<sup>45</sup>ATH residual chars  
426 (500 °C).

427 A peak at 1600 cm<sup>-1</sup> is the bending vibration of the water molecule adsorbed onto the silica  
428 surface in the FTIR spectrum of the residue layer of PU foam/nSiO<sub>2</sub> nanocomposites with  
429 and without flame retardant additives. In addition, the IR spectrum of residue chars of the  
430 nanocomposite with DAP additive has a signal at the wave number of 1055–940 cm<sup>-1</sup>,  
431 which is characteristic for the P=O, P-O-P, and P-O-C vibrations that phosphoric acid  
432 and/or its derivatives produced during combustion [43].

433 The morphology of remaining residual chars after burning was analyzed by SEM to further  
434 clarify the distinction between the flame-retardant performance of ATH and DAP, as  
435 described in Figure 8.



a) PU-nSiO<sub>2</sub>

b) PU-nSiO<sub>2</sub>/DAP

c) PU-nSiO<sub>2</sub>/ATH

436

437 **Figure 8.** SEM images of PU-nSiO<sub>2</sub>, PU-nSiO<sub>2</sub>/<sup>25</sup>DAP, and PU-nSiO<sub>2</sub>/<sup>45</sup>ATH residual chars

438

(500 °C).

439 Accordingly, after burning, the cell structure of the nanocomposite without flame retardant

440 was destroyed by the flame (Figure 8a). The SEM of residue char image of the

441 nanocomposite samples introduced DAP or ATH demonstrates the distinction with the

442 material without additive. Due to the presence of DAP, a thick layer of thermally stable char

443 has formed (with P<sub>4</sub>O<sub>10</sub> playing a key role), shielding the underlying material from thermal

444 deterioration (Figure 8b). Meanwhile, with the sample containing the ATH flame retardant

445 additive, the residual char layer became denser (Figure 8c), caused by the formation of

446 aluminum oxide which acts as a thermal barrier, helping to improve the fire resistance of the

447 nanocomposite. It is clear from the TGA data, FTIR, and SEM images that the two FRs,

448 DAP and ATH, have different flame-retardant mechanisms. With DAP, the flame-retardant

449 process occurs in both condensed phase and gas phase mechanisms. In the solid phase, DAP

450 is thermally decomposed to produce phosphoric acid. Phosphoric acids, after that, will react

451 with each other to produce a solid layer of P<sub>4</sub>O<sub>10</sub> that acts as a barrier to protect the material

452 from thermal degradation. In the gas phase, DAP is decomposed to produce phosphorus free

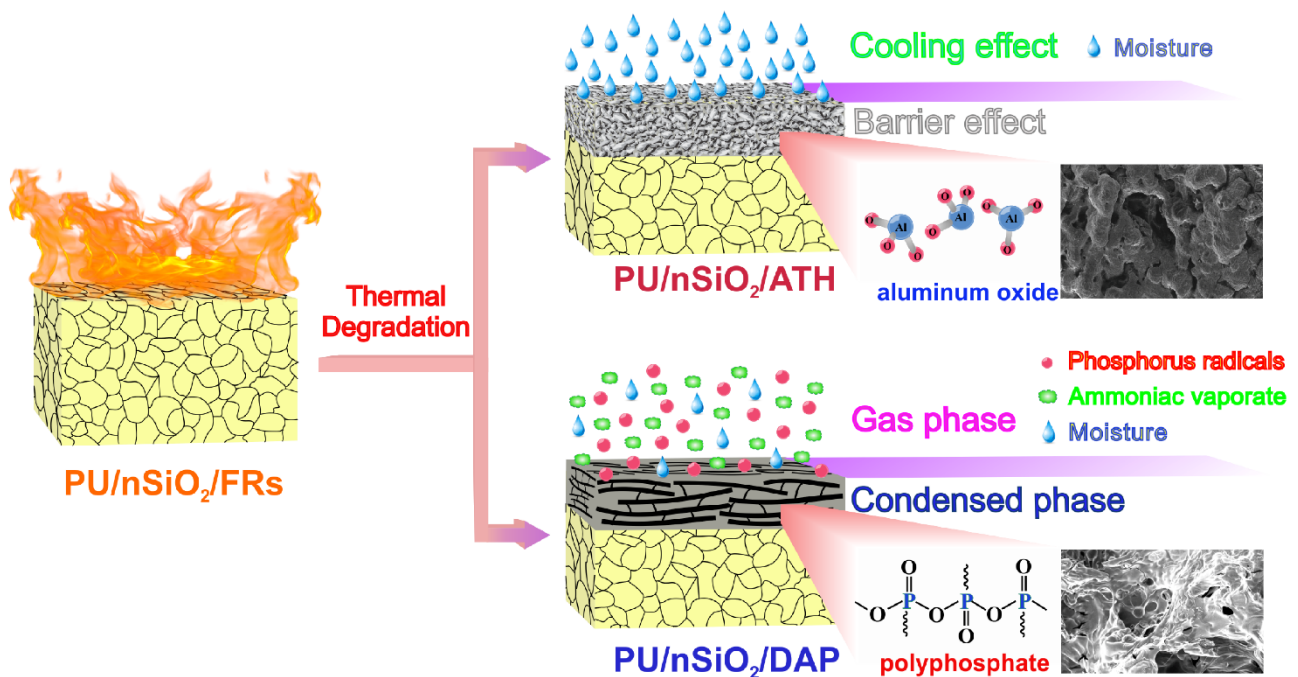
453 radicals such as PO• and PO<sub>2</sub>• which capture OH• and H• free radicals, resulting in a

454 significant improvement in fire resistance. Besides, the decomposition process of the DAP

455 flame retardant additive also produces NH<sub>3</sub> gas to help dilute and reduce the concentration

456 of highly active free radicals in the burning zone [43]. With the ATH, the flame-retardant  
 457 process mainly occurs through the thermal decomposition of the ATH additive. Aluminum  
 458 oxide is formed in significant quantities during this process, producing a barrier effect. In  
 459 addition, since the thermal decomposition of ATH is endothermic, it contributes to the fire  
 460 resistance of the material through its dilution and cooling effects [44].

461 Figure 9 schematizes the flame-retardant mechanism of two additives ATH and DAP,  
 462 employed in this research. It is clear that the two additives, ATH and DAP, differ in how  
 463 they perform as flame retardants, and, as a result, different amounts of flame retardant must  
 464 be employed to comply with the UL-94 V-0 fire retardant standard (25 phr for DAP and 45  
 465 phr for ATH).



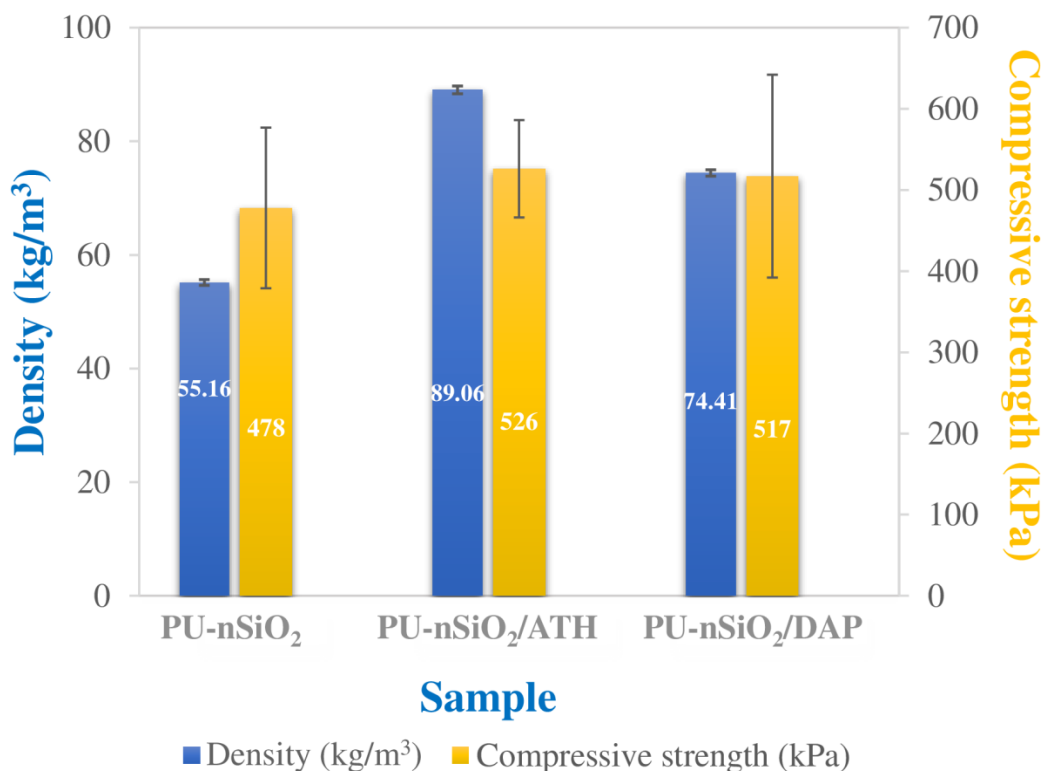
466

467 Figure 9: Flame retardant mechanism of PU-nSiO<sub>2</sub> with ATH or DAP additives.

### 468 3.5. Compressive strength

469 The high FRs loading often affect the mechanical properties of the nanocomposites. Thus,  
 470 evaluating the mechanical properties, or more especially the compressive strength of the  
 471 nanocomposites, is required to determine their applicability. With the presence of FRs, the

472 compressive strength of the nanocomposites increased by 8% and 10% respectively with the  
473 sample containing DAP at 25 phr and ATH at 45 phr, as presented in Figure 10.



474

475 Figure 10: Compressive strength and density of PU-nSiO<sub>2</sub>, PU-nSiO<sub>2</sub>/<sup>25</sup>DAP, and PU-  
476 nSiO<sub>2</sub>/<sup>45</sup>ATH.

477 A remarkable result is that the density of the nanocomposites also increased with the  
478 amount of additives used. In addition, a noticeable trend is that when the FR loading  
479 increases, the nanocomposite density also increases (specifically,  $74.41 \pm 0.56 \text{ kg/m}^3$  when  
480 using 25 phr DAP and  $89.06 \pm 0.56 \text{ kg/m}^3$  when using 45 phr ATH). During the foaming  
481 process, the presence of FRs increases the viscosity of the reaction mixture, which decreases  
482 the mobility of the molecules, slows the pace of PU polymerization, and reduces volume  
483 expansion, leading to the enhanced density of the PU foams.

484

485 To thoroughly analyze and explain the compressive strength and density of the  
486 nanocomposites, the pore structure of the samples was characterized by SEM, as shown in  
487 Figure 11. The cells in the nanocomposite sample made without additives are all oval in  
488 shape, and fairly homogeneous in size (191  $\mu\text{m}$  ca.), especially all cells are closed. In  
489 particular, from Figure 11 (a, a', a''), it can be seen that  $\text{nSiO}_2$  is dispersed quite well in the  
490 foam material,  $\text{nSiO}_2$  is mostly located in the cell walls, struts, and struts joints. This  
491 outcome is due to the effectively carried out  $\text{nSiO}_2$  dispersion procedure and the very low  
492 loading of  $\text{nSiO}_2$  (only 3wt%) that was utilized. For the PU- $\text{nSiO}_2$  sample containing ATH,  
493 although closed cells are still obtained, the cell size has increased (ca. 297  $\mu\text{m}$ ), along with  
494 the uniformity of the cells has decreased. The cell walls, struts, and strut joints were where  
495 the majority of the ATH FR was distributed (Figure 11 (b, b', b'')). However, the cell wall  
496 thickens and the cell size increases as a result of the high loading of ATH additive (45 phr).  
497 When the DAP was added to the PU- $\text{nSiO}_2$  material, similar outcomes were also seen; the  
498 additive was primarily distributed throughout the cell walls, struts, and struts joints (Figure  
499 11 (c, c', c'')). However, the DAP loading which is lower than the ATH (25 phr and 45 phr,  
500 respectively), has less of the impact on cell size and uniformity. In particular, compared to  
501 the PU- $\text{nSiO}_2$ /ATH sample, the average cell size of PU- $\text{nSiO}_2$ /DAP is smaller (ca. 275  $\mu\text{m}$ ),  
502 and the cells of PU foam nanocomposite with DAP are more uniform. The shape and  
503 structure of the cell are significantly changed by the flame retardant additive TPP. The  
504 PU/ $\text{nSiO}_2$ -TPP sample shrank after the synthesis and its cells did not maintain a stable  
505 structure (Figure 11 (d, d', d'')). The TPP component, in addition to its fireproof function,  
506 also has a plasticizing effect, which explains this phenomenon [38].

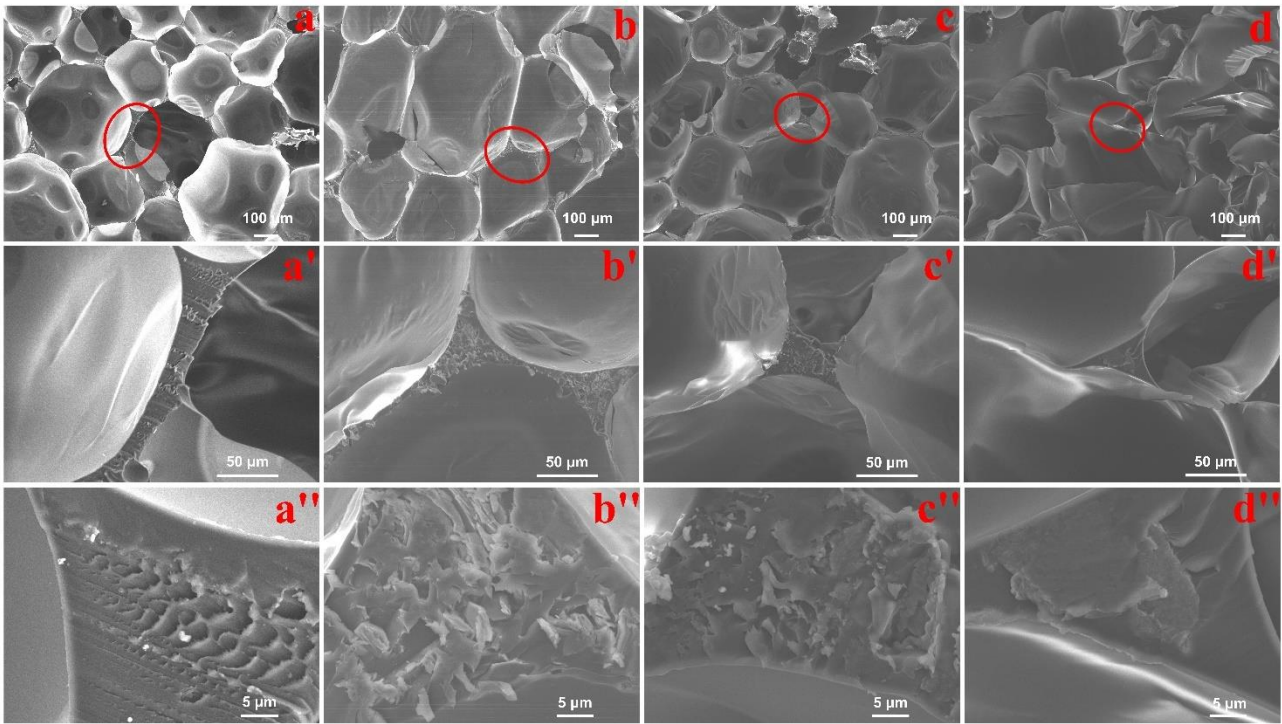
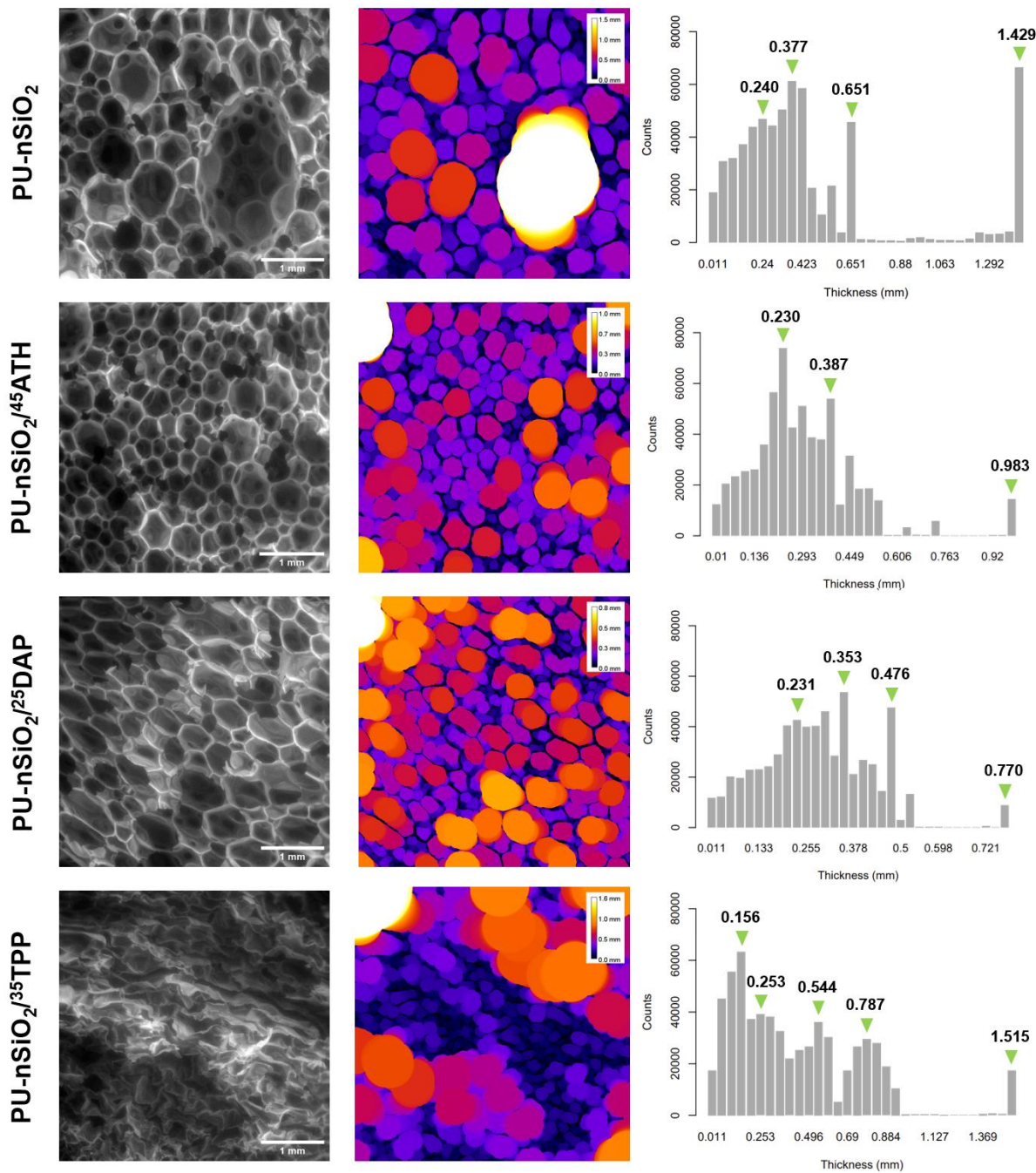


Figure 11: SEM images at different magnifications of PU-nSiO<sub>2</sub> (a, a', a''), PU-nSiO<sub>2</sub>/ATH (b, b', b''), PU-nSiO<sub>2</sub>/DAP (c, c', c''), and PU-nSiO<sub>2</sub>/TPP (d, d', d'').

507 Although the addition of FRs altered the size and shape of cells, it is not possible to see the  
 508 additive's agglomeration, which disturbed the cell's structure observed from the SEM  
 509 image. This implies that the additives were well dispersed into the material throughout the  
 510 mixing process and were mostly embedded into the pore wall, improving the material's  
 511 compressive strength. Additionally, it was observed that while the density of the material  
 512 exhibited a notable increase, there was not a significant enhancement in compressive  
 513 strength. As discussed previously, higher loadings of FRs were associated with expanded  
 514 cell size, changing cell shape, and thinner cell walls (Figure 11), leading to limit the  
 515 material's ability to withstand external forces, even though the density increased due to the  
 516 addition of the FRs.

517 In addition, the pore structure of the samples was characterized by ESEM, as shown in  
 518 Figure 12. Pore size distribution was estimated by generating thickness maps, that is,  
 519 measuring the diameter of the largest circles that can be fit inside the pores.



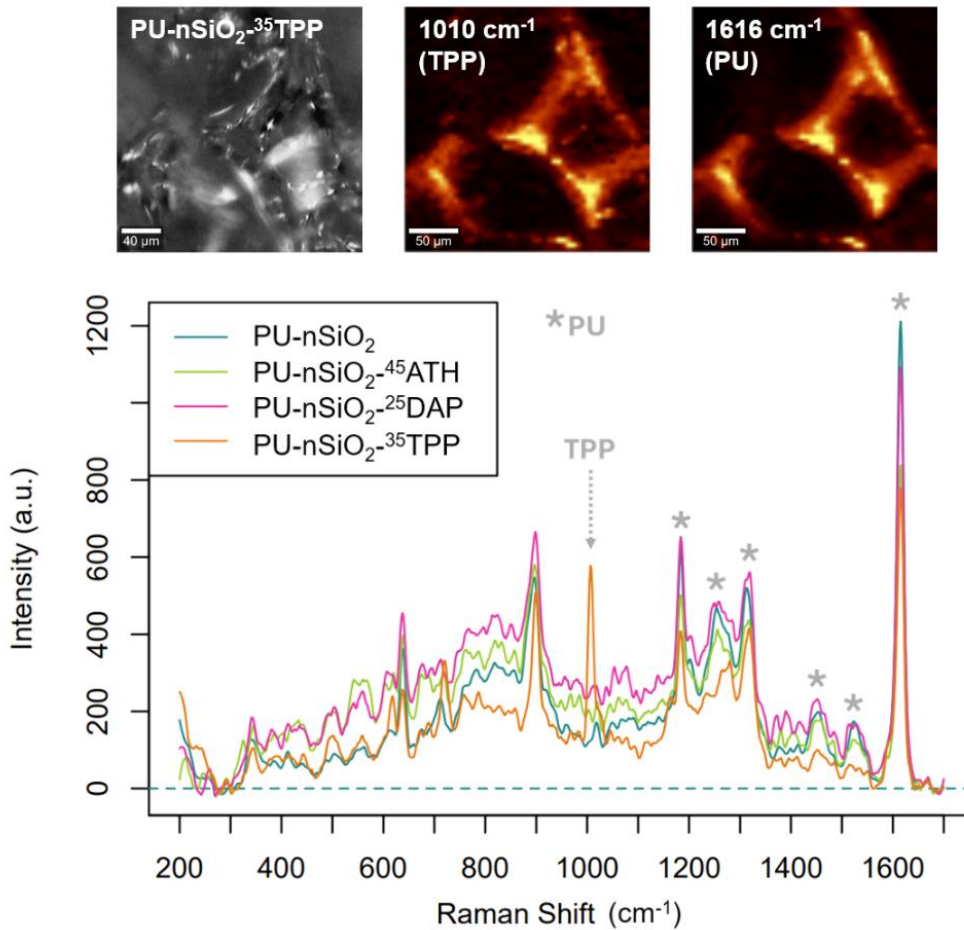
520  
 521 Figure 12. SEM images of PU-nSiO<sub>2</sub>, PU-nSiO<sub>2</sub>/<sup>45</sup>ATH, PU-nSiO<sub>2</sub>/<sup>25</sup>DAP, and PU-  
 522 nSiO<sub>2</sub>/<sup>35</sup>TPP samples (left). Thickness maps (mm) generated in FIJI (middle) and their  
 523 respective histograms (right).

524 Except for the PU-nSiO<sub>2</sub>/<sup>35</sup>TPP sample, in which pores are collapsed, the composites  
525 present a closed-cell pore structure with ellipsoidal pores. Pore collapse may be a result of  
526 the presence of TPP and its plasticizing action, making the cell walls more ductile, i.e.,  
527 increasing their deformation before fracture. The addition of ATH or DAP appeared to  
528 hinder the formation of the larger pores observed for the PU-nSiO<sub>2</sub> sample, probably due to  
529 a partial limitation of the porosity reaction during material synthesis. As a result, the pore  
530 size distribution is more homogeneous, what may be linked to the improved compressive  
531 strength measured for the PU-nSiO<sub>2</sub>/<sup>45</sup>ATH and PU-nSiO<sub>2</sub>/<sup>25</sup>DAP samples.

532 In addition, no agglomerates of additives could be observed, indicating an even dispersion  
533 over the pore cell walls. This result was confirmed by Raman spectroscopy, as illustrated in  
534 Figure 13. Characteristic vibrations from polyurethane could be identified at 1184, 1256,  
535 1314, 1450, 1528 and 1616 cm<sup>-1</sup> [45, 46]. The spectra for PU-nSiO<sub>2</sub>, PU-nSiO<sub>2</sub>/<sup>45</sup>ATH, and  
536 PU-nSiO<sub>2</sub>/<sup>25</sup>DAP presented a similar spectral profile, with no additional peaks due to the  
537 presence of the additives. The spectra were obtained using a 785 nm laser and a 10x  
538 objective of NA = 0.25, providing a lateral resolution of approximately 1.9 μm according to  
539 Rayleigh criterion ( $0.61 * (\lambda/NA)$ ). On this basis, no micrometric agglomerates of additives  
540 could be identified on the samples.

541 The PU-nSiO<sub>2</sub>/<sup>35</sup>TPP sample, on the other hand, presented a new peak at 1010 cm<sup>-1</sup>,  
542 corresponding to the ring symmetric stretching from triphenyl phosphate [47]. The  
543 hyperspectral maps for the 1010 and 1616 cm<sup>-1</sup> (C=C stretching from aromatic rings in PU)  
544 peaks coincide, also demonstrating an even dispersion of the additive over the pore cell  
545 walls.

546



547

548 Figure 13. Raman spectra for PU-nSiO<sub>2</sub>, PU-nSiO<sub>2</sub>/<sup>45</sup>ATH, PU-nSiO<sub>2</sub>/<sup>25</sup>DAP, and PU-  
 549 nSiO<sub>2</sub>/<sup>35</sup>TPP samples (bottom). Optical microscopy and Raman images for PU-nSiO<sub>2</sub>/<sup>35</sup>TPP  
 550 sample (top).

551

### 552 3.6. Thermal conductivity

553 The important characteristic of PU foams and its nanocomposites is their effective thermal  
 554 conductivities, as shown in Table 3. Accordingly, the PU-nSiO<sub>2</sub> sample has the most  
 555 effective thermal insulation performance with the lowest thermal conductivity value, about  
 556 0.036 W.m<sup>-1</sup>.K<sup>-1</sup>, corresponding to a density of about 55.2 (kg/m<sup>3</sup>). The addition of different  
 557 flame-retardant additives to sample PU-nSiO<sub>2</sub> at different concentrations leads to slight  
 558 increasing the thermal conductivity value to about 0.042 W.m<sup>-1</sup>.K<sup>-1</sup> of PU-nSiO<sub>2</sub>/<sup>25</sup>DAP,  
 559 0.044 W.m<sup>-1</sup>.K<sup>-1</sup> of PU-nSiO<sub>2</sub>/<sup>45</sup>ATH and 0.047 W.m<sup>-1</sup>.K<sup>-1</sup> of PU-nSiO<sub>2</sub>/<sup>35</sup>TPP, respectively,

560 corresponding to a slight increase in their density. This result can be explained by the fact  
 561 that the flame-retardant additives are inorganic compounds with higher density and thermal  
 562 conductivity than the PU-nSiO<sub>2</sub> sample.

563 Compared to PU foams reinforced by bamboo fiber and bamboo nanocellulose fiber in the  
 564 literature, the PU-nSiO<sub>2</sub> sample and its nanocomposites in this study demonstrated their  
 565 higher thermal insulation efficiency thanks to their lower values of thermal conductivity  
 566 without significantly changing their densities, as presented in Table 3. Furthermore,  
 567 compared to insulation panels derived from natural fibers, the PU-nSiO<sub>2</sub> sample and its  
 568 nanocomposites have superior thermal insulation properties. This result can be explained by  
 569 their highly porous structure, which contains the air within the pores, leading to their low  
 570 thermal conductivity values. These materials have therefore demonstrated significant  
 571 thermal insulation performance and are promising for industrial applications.

572 Table 3: Thermal conductivity of PU-nSiO<sub>2</sub> and its nanocomposites

Sample	Density (kg/m <sup>3</sup> )	Thermal conductivity (W.m <sup>-1</sup> .K <sup>-1</sup> )	Ref.
PU-nSiO <sub>2</sub>	55.2	0.036 ± 0.001	This study
PU-nSiO <sub>2</sub> /45ATH	89.1	0.044 ± 0.001	This study
PU-nSiO <sub>2</sub> /25DAP	74.4	0.042 ± 0.001	This study
PU-nSiO <sub>2</sub> /35TPP		0.047 ± 0.001	This study
PU foams/7% bamboo nanocellulose fiber	76.2 ± 3.8	0.0489	[48]
PU foams/7% bamboo nanocellulose fiber	82.4 ± 4.3	0.0484	[48]

PU foams/7% bamboo fiber	81.7 ± 5.3	0.0491	[48]
PU foams/5% bamboo fiber	82.1 ± 3.4	0.0510	[48]
Hemp fibers (48%), Shives (32%) and binder fibers (bicomponent fibers) (20%)	30	0.05	[49]
Cotton stalks fiberboard	150–450	0.059–0.082	[50]
Bamboo fiberboard	431	0.077	[51]
Bamboo powder board	628	0.101	[52]

573

#### 574 **4. Conclusion**

575 This work investigated the effect of DAP or ATH additives on the flame retardancy, thermal  
576 properties, and mechanical properties of PU foam/nSiO<sub>2</sub> nanocomposites. With the presence  
577 of DAP (25 phr) or ATH (45 phr), the nanocomposites were able to meet the UL-94 V-0  
578 standard. The results of the LOI analysis also revealed that the addition of DAP increased  
579 the LOI value of nanocomposites by 30%, reaching a value of 26% (as compared to 20% of  
580 the sample without the additive). The TGA analysis method also showed a significant  
581 improvement in the thermal properties of the nanocomposites in the presence of FRs.  
582 Notably, the amount of residual char at 800 °C increased by 100% and 120%, respectively,  
583 with ATH and DAP additives. In addition, the presence of FRs also increases the  
584 compressive strength values by 8% and 10% respectively with the presence of DAP and  
585 ATH in the nanocomposite, namely thanks to an increased density. Particularly, this work  
586 proved that the two additives, DAP and ATH, have different flame-retardant mechanisms  
587 based on the difference in the amount of additives required for the material to meet the UL-  
588 94 V-0 fireproof standard as well as the results of the FTIR and SEM, performed on the

589 residue char layer after burning. In addition, DAP acts as a condensed phase and gas phase  
590 mechanism while ATH plays the role of the barrier layer to the heat flux. In particular, PU-  
591 SiO<sub>2</sub> and its nanocomposites have low thermal conductivity values, which demonstrate high  
592 thermal insulation efficiency compared to other bio-insulation materials. In addition, the  
593 addition of FRs to the sample leads to an increase in the thermal conductivity compared to  
594 samples without FRs, but the thermal conductivity value of these samples is still much  
595 lower than samples of the same density in the literature.

#### 596 **Declaration of competing interest**

597 The authors declare that they have no known competing financial interests or personal  
598 relationships that could have appeared to influence the work reported in this paper.

#### 599 **Acknowledgments**

600 This research is funded by Vietnam National University Ho Chi Minh City (VNU-HCM)  
601 under grant number C2022-18-41.

#### 602 **References**

- 603 [1] A. Navidfar, L. Trabzon, Fabrication and characterization of polyurethane hybrid  
604 nanocomposites: mechanical, thermal, acoustic, and dielectric properties, *Emergent*  
605 *Materials* 5(4) (2022) 1157-1165.
- 606 [2] Y. Chen, M. Li, F. Hao, C. Yang, Enhanced flame retardant performance of rigid  
607 polyurethane foam by using the modified OMMT layers with large surface area and  
608 ammonium polyphosphate, *Materials Today Communications* 32 (2022) 104121.
- 609 [3] M. Zhu, Z. Ma, L. Liu, J. Zhang, S. Huo, P. Song, Recent advances in fire-retardant  
610 rigid polyurethane foam, *Journal of Materials Science & Technology* 112 (2022) 315-328.

- 611 [4] X.-L. Chen, F.-R. Zeng, W.-X. Li, L. Zhang, C. Deng, Y. Tan, M.-J. Chen, S.-C. Huang,  
612 B.-W. Liu, Y.-Z. Wang, H.-B. Zhao, Durable flame-retardant, smoke-suppressant, and  
613 thermal-insulating biomass polyurethane foam enabled by a green bio-based system, *Journal*  
614 *of Materials Science & Technology* 162 (2023) 179-188.
- 615 [5] T.A. Nguyen, T.M.N. Ha, B.T. Nguyen, D. Ha, T. Vu Vo, D.M. Nguyen, D.K. Vo, N.T.  
616 Nguyen, T.V. Nguyen, D. Hoang, Microwave-assisted polyol liquefaction from bamboo for  
617 bio-polyurethane foams fabrication, *Journal of Environmental Chemical Engineering* 11(2)  
618 (2023) 109605.
- 619 [6] J. Wang, B. Xu, X. Wang, Y. Liu, A phosphorous-based bi-functional flame retardant  
620 for rigid polyurethane foam, *Polymer Degradation and Stability* 186 (2021) 109516.
- 621 [7] J. Yan, P. Xu, P. Zhang, H. Fan, Surface-modified ammonium polyphosphate for flame-  
622 retardant and reinforced polyurethane composites, *Colloids and Surfaces A:*  
623 *Physicochemical and Engineering Aspects* 626 (2021) 127092.
- 624 [8] X. Wang, P. Zhang, Z. Huang, W. Xing, L. Song, Y. Hu, Effect of aluminum  
625 diethylphosphinate on the thermal stability and flame retardancy of flexible polyurethane  
626 foams, *Fire Safety Journal* 106 (2019) 72-79.
- 627 [9] B.-W. Liu, H.-B. Zhao, Y.-Z. Wang, *Advanced Flame-Retardant Methods for Polymeric*  
628 *Materials*, *Advanced Materials* 34(46) (2022) 2107905.
- 629 [10] Y. Yuan, W. Wang, Y. Xiao, A. Chun Yin Yuen, L. Mao, H. Pan, B. Yu, Y. Hu,  
630 Surface modification of multi-scale cuprous oxide with tunable catalytic activity towards  
631 toxic fumes and smoke suppression of rigid polyurethane foam, *Applied Surface Science*  
632 556 (2021) 149792.

- 633 [11] H. Zhu, S. Xu, Preparation of Flame-Retardant Rigid Polyurethane Foams by  
634 Combining Modified Melamine-Formaldehyde Resin and Phosphorus Flame Retardants,  
635 ACS omega 5(17) (2020) 9658-9667.
- 636 [12] J. Zhang, F. Zeng, B. Liu, Z. Wang, X. Lin, H. Zhao, Y. Wang, A biomimetic closed-  
637 loop recyclable, long-term durable, extreme-condition resistant, flame-retardant nanocoating  
638 synthesized by reversible flocculation assembly, Materials Horizons 10(10) (2023) 4551-  
639 4561.
- 640 [13] F. Zeng, X. Men, M. Chen, B. Liu, Q. Han, S. Huang, H. Zhao, Y. Wang, Molecular-  
641 micron multiscale toughening and flame retarding for polyurethane foams, Chemical  
642 Engineering Journal 454 (2023) 140023.
- 643 [14] Q. Zhao, C. Chen, R. Fan, Y. Yuan, Y. Xing, X. Ma, Halogen-free flame-retardant  
644 rigid polyurethane foam with a nitrogen–phosphorus flame retardant, Journal of Fire  
645 Sciences 35(2) (2017) 99-117.
- 646 [15] Z. Lin, Q. Zhao, R. Fan, X. Yuan, F. Tian, Flame retardancy and thermal properties of  
647 rigid polyurethane foam conjugated with a phosphorus–nitrogen halogen-free intumescent  
648 flame retardant, Journal of Fire Sciences 38(3) (2020) 235-252.
- 649 [16] C. Liu, P. Zhang, Y. Shi, X. Rao, S. Cai, L. Fu, Y. Feng, L. Wang, X. Zheng, W. Yang,  
650 Enhanced Fire Safety of Rigid Polyurethane Foam via Synergistic Effect of  
651 Phosphorus/Nitrogen Compounds and Expandable Graphite, Molecules, 2020.
- 652 [17] W. Lu, Z. Jin, Synthesis of phosphorus/nitrogen containing intumescent flame  
653 retardants from p-hydroxybenzaldehyde, vanillin and syringaldehyde for rigid polyurethane  
654 foams, Polymer Degradation and Stability 195 (2022) 109768.

- 655 [18] S. Członka, A. Strąkowska, K. Strzelec, A. Kairyte, A. Kremensas, Melamine, silica,  
656 and ionic liquid as a novel flame retardant for rigid polyurethane foams with enhanced  
657 flame retardancy and mechanical properties, *Polymer Testing* 87 (2020) 106511.
- 658 [19] L. Verdolotti, M. Oliviero, M. Lavorgna, C. Santillo, F. Tallia, S. Iannace, S. Chen,  
659 J.R. Jones, “Aerogel-like” polysiloxane-polyurethane hybrid foams with enhanced  
660 mechanical and thermal-insulating properties, *Composites Science and Technology* 213  
661 (2021) 108917.
- 662 [20] B.A. Goodman, Utilization of waste straw and husks from rice production: A review,  
663 *Journal of Bioresources and Bioproducts* 5(3) (2020) 143-162.
- 664 [21] S. Steven, E. Restiawaty, Y. Bindar, Routes for energy and bio-silica production from  
665 rice husk: A comprehensive review and emerging prospect, *Renewable and Sustainable*  
666 *Energy Reviews* 149 (2021) 111329.
- 667 [22] H. Moayedi, B. Aghel, M.a.M. Abdullahi, H. Nguyen, A. Safuan A Rashid,  
668 Applications of rice husk ash as green and sustainable biomass, *Journal of Cleaner*  
669 *Production* 237 (2019) 117851.
- 670 [23] V.B. Carmona, R.M. Oliveira, W.T.L. Silva, L.H.C. Mattoso, J.M. Marconcini,  
671 Nanosilica from rice husk: Extraction and characterization, *Industrial Crops and Products* 43  
672 (2013) 291-296.
- 673 [24] G. Chen, S. Zhou, G. Gu, L. Wu, Modification of colloidal silica on the mechanical  
674 properties of acrylic based polyurethane/silica composites, *Colloids and Surfaces A:*  
675 *Physicochemical and Engineering Aspects* 296(1) (2007) 29-36.
- 676 [25] G. Leder, T. Ladwig, V. Valter, S. Frahn, J. Meyer, New effects of fumed silica in  
677 modern coatings, *Progress in Organic Coatings* 45(2) (2002) 139-144.

- 678 [26] A. Nodera, T. Kanai, Flame retardancy of polycarbonate–polydimethylsiloxane block  
679 copolymer/silica nanocomposites, *Journal of Applied Polymer Science* 101(6) (2006) 3862-  
680 3868.
- 681 [27] T. Kashiwagi, A.B. Morgan, J.M. Antonucci, M.R. VanLandingham, R.H. Harris Jr,  
682 W.H. Awad, J.R. Shields, Thermal and flammability properties of a silica–  
683 poly(methylmethacrylate) nanocomposite, *Journal of Applied Polymer Science* 89(8) (2003)  
684 2072-2078.
- 685 [28] M.H. Moghim, M. Keshavarz, S.M. Zebarjad, Effect of SiO<sub>2</sub> nanoparticles on  
686 compression behavior of flexible polyurethane foam, *Polymer Bulletin* 76(1) (2019) 227-  
687 239.
- 688 [29] X.g. Zheng, Q. Dong, X. Wang, P. Yu, W. Wang, J. Zhang, L. Ren, Improvement of  
689 Flame Retardancy of Polyurethane Foam Using DOPO-Immobilized Silica Aerogel, 8  
690 (2021).
- 691 [30] K. Takashi, G. Jeffrey, B. Kathryn, H. Richard, S. John, A. Asano, Flame Retardant  
692 Mechanism of Silica Gel/Silica, (2000).
- 693 [31] S.H. Lee, S.G. Lee, J.S. Lee, B.C. Ma, Understanding the Flame Retardant Mechanism  
694 of Intumescent Flame Retardant on Improving the Fire Safety of Rigid Polyurethane Foam,  
695 *Polymers*, 2022.
- 696 [32] C.T. Pham, B.T. Nguyen, H.T.Q. Phan, L.H. Pham, C.N. Hoang, N.N. Nguyen, P.-C.  
697 Lee, S.-J. Kang, J. Kim, D. Hoang, Highly efficient fire retardant behavior, thermal  
698 stability, and physicomechanical properties of rigid polyurethane foam based on recycled  
699 poly(ethylene terephthalate), *Journal of Applied Polymer Science* 137(37) (2020) 49110.
- 700 [33] L.H. Pham, L.T. Pham, D. Hoang, J. Kim, Effective Phosphorus/Phosphorus-Nitrogen  
701 Fire Retardants Applied to Biocomposites Based on Polypropylene-Wood Flour:

702 Flammability, Thermal Behavior, and Mechanical Properties, *Macromolecular Research*  
703 27(12) (2019) 1185-1192.

704 [34] N.T. Nguyen, D.H. Nguyen, D.D. Pham, V.P. Dang, Q.H. Nguyen, D.Q. Hoang, New  
705 oligochitosan-nanosilica hybrid materials: preparation and application on chili plants for  
706 resistance to anthracnose disease and growth enhancement, *Polymer Journal* 49(12) (2017)  
707 861-869.

708 [35] L. Terrei, Z. Acem, V. Georges, P. Lardet, P. Boulet, G. Parent, Experimental tools  
709 applied to ignition study of spruce wood under cone calorimeter, *Fire Safety Journal* 108  
710 (2019) 102845.

711 [36] I. DIS, Fire tests–Reaction to fire–rate of heat release from building products,  
712 International Organization for Standardization (1990).

713 [37] J. Schindelin, I. Arganda-Carreras, E. Frise, V. Kaynig, M. Longair, T. Pietzsch, S.  
714 Preibisch, C. Rueden, S. Saalfeld, B. Schmid, J.-Y. Tinevez, D.J. White, V. Hartenstein, K.  
715 Eliceiri, P. Tomancak, A. Cardona, Fiji: an open-source platform for biological-image  
716 analysis, *Nature Methods* 9(7) (2012) 676-682.

717 [38] S.V. Beleites C, HyperSpec: a package to handle hyperspectral data sets in R. R  
718 package version 0.100.0.

719 [39] I.J. Fernandes, D. Calheiro, A.G. Kieling, C.A.M. Moraes, T.L.A.C. Rocha, F.A.  
720 Brehm, R.C.E. Modolo, Characterization of rice husk ash produced using different biomass  
721 combustion techniques for energy, *Fuel* 165 (2016) 351-359.

722 [40] S.R. Darmakkolla, H. Tran, A. Gupta, S.B. Rananavare, A method to derivatize surface  
723 silanol groups to Si-alkyl groups in carbon-doped silicon oxides, *RSC Advances* 6(95)  
724 (2016) 93219-93230.

- 725 [41] G. Wardhani, N. Nurlela, M. Azizah, Silica Content and Structure from Corncob Ash  
726 with Various Acid Treatment (HCl, HBr, and Citric Acid), *Molekul* 12 (2017) 174.
- 727 [42] C. Wang, J. Wang, Z. Men, Y. Wang, Z. Han, Thermal Degradation and Combustion  
728 Behaviors of Polyethylene/Alumina Trihydrate/Graphene Nanoplatelets, *Polymers*, 2019.
- 729 [43] D. Hoang, T. Pham, T. Nguyen, H. An, J. Kim, Organo-Phosphorus Flame Retardants  
730 for Poly(vinyl chloride)/Wood Flour Composite, *Polymer Composites* 39(3) (2018) 961-  
731 970.
- 732 [44] H. Phan, B. Nguyen, L. Phạm, C. Pham, D. Vi, C. Hoang Ngoc, N. Nguyen, J. Kim, D.  
733 Hoang, Excellent Fireproof Characteristics and High Thermal Stability of Rice Husk-Filled  
734 Polyurethane with Halogen-Free Flame Retardant, *Polymers* 11 (2019) 1587.
- 735 [45] S. França de Sá, J.L. Ferreira, A.S. Matos, R. Macedo, A.M. Ramos, A new insight into  
736 polyurethane foam deterioration – the use of Raman microscopy for the evaluation of long-  
737 term storage conditions, *Journal of Raman Spectroscopy* 47(12) (2016) 1494-1504.
- 738 [46] S. Parnell, K. Min, M. Cakmak, Kinetic studies of polyurethane polymerization with  
739 Raman spectroscopy, *Polymer* 44(18) (2003) 5137-5144.
- 740 [47] K. Ciosek Högström, H. Lundgren, S. Wilken, T.G. Zavalis, M. Behm, K. Edström, P.  
741 Jacobsson, P. Johansson, G. Lindbergh, Impact of the flame retardant additive triphenyl  
742 phosphate (TPP) on the performance of graphite/LiFePO<sub>4</sub> cells in high power applications,  
743 *Journal of Power Sources* 256 (2014) 430-439.
- 744 [48] C. Qiu, F. Li, L. Wang, X. Zhang, Y. Zhang, Q. Tang, X. Zhao, C.F. De Hoop, X.  
745 Peng, X. Yu, X. Huang, The preparation and properties of polyurethane foams reinforced  
746 with bamboo fiber sources in China, *Materials Research Express* 8(4) (2021) 045501.

- 747 [49] A. Korjenic, J. Zach, J. Hroudová, The use of insulating materials based on natural  
748 fibers in combination with plant facades in building constructions, *Energy and Buildings*  
749 116 (2016) 45-58.
- 750 [50] X.-y. Zhou, F. Zheng, H.-g. Li, C.-l. Lu, An environment-friendly thermal insulation  
751 material from cotton stalk fibers, *Energy and Buildings* 42(7) (2010) 1070-1074.
- 752 [51] D.M. Nguyen, A.-C. Grillet, T.M.H. Diep, C.N. Ha Thuc, M. Woloszyn, Hygrothermal  
753 properties of bio-insulation building materials based on bamboo fibers and bio-glues,  
754 *Construction and Building Materials* 155 (2017) 852-866.
- 755 [52] D.M. Nguyen, A.-C. Grillet, Q.-B. Bui, T.M.H. Diep, M. Woloszyn, Building bio-  
756 insulation materials based on bamboo powder and bio-binders, *Construction and Building*  
757 *Materials* 186 (2018) 686-698.
- 758